Numerical evaluation of subsurface soil water evaporation derived from sensible heat balance

Masaru Sakai,[1] Scott B. Jones,[1] and Markus Tuller[2]

[1]   A recently introduced measurement approach allows in situ determination of subsurface soil water evaporation by means of heat-pulse probes (HPP). The latent heat component of subsurface evaporation is estimated from the residual of the sensible heat balance. This heat balance method requires measurement of vertical soil temperature and estimates of thermal properties for soil water evaporation determination. Our objective was to employ numerically simulated thermal and hydraulic processes using constant or diurnally cycled surface boundary conditions to evaluate and understand this technique. Three observation grid spacings, namely, 6 mm (tri-needle HPP), 3 mm (penta-needle HPP) and 1 mm, along with three soil textures (sand, silt, and silty clay) were used to test the heat balance method. The comparison of heat balance–based evaporation rate estimates with an independent soil profile water balance revealed substantial errors when thermal conductivity (λ) was averaged spatially across the evaporation front. Since the conduction component of heat flux is the dominant process at the evaporation front, the estimation of evaporation rate was significantly improved using depth-dependent λ instead of a space-averaged λ. A near-surface "undetectable zone" exists, where the heat balance calculation is irreconcilable, resulting in underestimation of total subsurface evaporation. The method performs better for medium- and coarse-textured soils than for fine-textured soils, where portions of the drying front may be maintained longer within the undetectable zone. Using smaller temperature sensor spacing near the soil surface minimized underestimation from the undetectable zone and improved accuracy of total subsurface evaporation rate estimates.

1. Introduction

[2] Soil water evaporation is a key process for water exchange between soil and the atmosphere; it is involved in plant physiological functioning and affects the amount of available water for plants and microorganisms inhabiting the soil. Bare soil evaporation and plant–soil–atmospheric interactions are important components of the water balance in semiarid and arid regions. Drying and evaporation processes are also of interest for many engineering and industrial applications, such as food processing and preservation, production of ceramics and paper, eye and skin care, and numerous construction activities [*Lehmann et al.*, 2008]. Because it is difficult to directly measure evaporation rates from soils with the exception of using lysimeters [*Evett et al.*, 1995], the options are limited to indirect methods such as the Bowen ratio–energy balance or the eddy covariance method [*Warrick*, 2002]. Although numerical simulation models for soil water flow and heat transport allow

calculation of evaporation rates from variably saturated soils [*Saito et al.*, 2006], determination of the required thermal and hydraulic soil properties for model parameterization is laborious.

[3] The rate of soil evaporation is affected by both atmospheric demand (humidity, temperature, and velocity of ambient air) and soil pore space and transport properties (thermal and hydraulic conductivities and vapor diffusivity). This complexity leads to highly dynamic interactions between media properties, transport processes and boundary conditions and results in a broad range of evaporation behaviors as discussed by *van Brakel* [1980] and *Prat* [2002]. Evaporation from soil surfaces involves mass and energy transport including phase change, vapor diffusion, and liquid flow resulting in complex displacement patterns that affect the drying rate, which varies with time. Soil water evaporation can be separated into two stages [*Jury and Horton*, 2004] with a relatively high and constant initial evaporation rate (stage 1) that is followed by a lower rate controlled by vapor diffusion (stage 2) [*Kaviany and Mittal*, 1987; *Salvucci*, 1997; *Schultz*, 1991; *van Brakel*, 1980]. During stage 1 the rate of water loss per unit surface area remains nearly constant and is close to the evaporation rate from a free water surface. The establishment of this nearly constant initial rate is notable considering the significant change of fluid distribution within the medium and the continuous retreat of the

---

[1]Department of Plants, Soils and Climate, Utah State University, Logan, Utah, USA.

[2]Department of Soil, Water and Environmental Science, University of Arizona, Tucson, Arizona, USA.

drying front [*van Brakel*, 1980; *Yamanaka and Yonetani*, 1999; *Shokri et al.*, 2009a, 2009b]. At a critical surface water content [*Keey*, 1972] or drying front depth [*Lehmann et al.*, 2008] the first stage abruptly ends and is followed by a lower rate stage that is primarily controlled by diffusive mass transfer [*Schultz*, 1991]. The conditions and mechanisms controlling drying from porous media are discussed in numerous studies [*Chen and Pei*, 1989; *Coumans*, 2000; *Lehmann et al.*, 2008; *Scherer*, 1990; *Schlünder*, 1988; *van Brakel*, 1980].

[4] Studies that are focused on subsurface soil heat balance including sensible heat flux, sensible heat storage, and latent heat of vaporization have been conducted by *Mayocchi and Bristow* [1995]. More recently *Heitman et al.* [2008a] introduced a heat balance technique to compute stage 2 evaporation rates from in situ heat-pulse probe (HPP) measurements. *Heitman et al.* [2008b] reported that daily subsurface evaporation computed with this method was in good agreement with Bowen ratio and microlysimeter estimates of subsurface evaporation rates.

[5] Though the accuracy of evaporation rate estimates depends on many factors like soil temperature observation spacing and soil texture, the theoretical limitations of the heat balance method have not been thoroughly evaluated. In general, the HPP allows measurement of thermal diffusivity, thermal conductivity, and soil water fluxes [e.g., *Bristow*, 1998; *Kluitenberg et al.*, 2007; *Yang and Jones*, 2009].

[6] There are a number of different HPP designs that have been previously employed for research. A dual-needle HPP with one heater needle and one temperature sensor needle with 6 mm separation distance was introduced by *Campbell et al.* [1991]. A tri-needle HPP with one heater needle and two temperature sensing needles with 6 mm spacing was developed by *Ren et al.* [2000]. More recently, a penta-needle HPP has been developed to determine two dimensional water fluxes. The spacing between the thermistor and heater needles of the penta-needle HPP designed by *Endo and Hara* [2007] was 10 mm, and the one used by *Yang and Jones* [2009] had 6.5 mm spacing. When one pair of opposing thermistor needles in the penta-needle HPP is rotated 27.3° from a vertical orientation and a thermistor is included within the heating needle, temperature measurements are provided every 2.98 mm within the soil profile. Very recently, novel attempts to provide finer thermistor spacings (i.e., 1 mm) at the soil surface area have been made.

[7] The objective of this study was to evaluate the applicability and potential limitations of the heat balance method for estimation of subsurface evaporation rates. This was accomplished by using numerically generated water contents, temperatures, and thermal properties during soil water evaporation, where both the water and heat balance were accurately accounted for and compared. Initially, simulations with constant atmospheric conditions driving evaporation were conducted in order to theoretically examine the impact of temperature sensor spacing and soil textures on sensible heat balance–based subsurface evaporation estimation without the complication of variable boundary conditions. In a second step, diurnal cycling of the energy inputs was employed as a means for assessing the applicability of the sensible heat balance method under field-simulated conditions.

2. Theoretical and Experimental Considerations

### 2.1. Model for Calculating Subsurface Evaporation Rate

[8] The heat-pulse technique is a well-known method for estimation of thermal properties in soils [*Bristow*, 1998]. Neighboring temperature sensors measure the heat-pulse response from a heater needle (Figure 1). By analyzing temperature rise, soil thermal diffusivity and thermal conductivity are estimated for the soil between the heater and temperature sensors. Soil heat capacity is obtained from a ratio of thermal diffusivity and thermal conductivity. *Heitman et al.* [2008a, 2008b] introduced a method for computation of subsurface evaporation rates based on the sensible heat balance determined from soil temperatures and soil thermal properties measured by heat-pulse probe (heat balance method, Figure 1):

$$LE = \left[\left(-\lambda \frac{T_i - T_{i+1}}{z_i - z_{i+1}} \right) - \left(-\lambda \frac{T_{i-1} - T_i}{z_{i-1} - z_i} \right) \right] - \Delta S, \quad (1)$$

where E is the subsurface evaporation rate (m s^{-1}), L is the volumetric latent heat of vaporization (J m^{-3}; $= 2.495 \times 10^9 - 2.247 \times 10^6 \, T$ [*Forsythe*, 1964]), λ is the soil thermal conductivity (W m^{-1} °C^{-1}), T is the soil temperature (°C), z is the depth in meters ($z = 0$ at the soil surface and is negative below the surface), the subscript i is an index variable related to the soil layer depth increment, and ΔS is the change in soil sensible heat storage (J m^{-2} s^{-1}), given as:

$$\Delta S = \sum_{i=1}^{N} C_i^{j-1} \frac{T_i^j - T_i^{j-1}}{t^j - t^{j-1}} (z_i - z_{i-1}), \quad (2)$$

with C as the volumetric heat capacity of moist soil (J m^{-3} °C^{-1}) at the previous time step, $j - 1$, t as time (s), and the superscript j as an index variable for the time step. Using HPP measurements, the average λ and C between neighboring temperature sensors can be obtained within a 12 mm
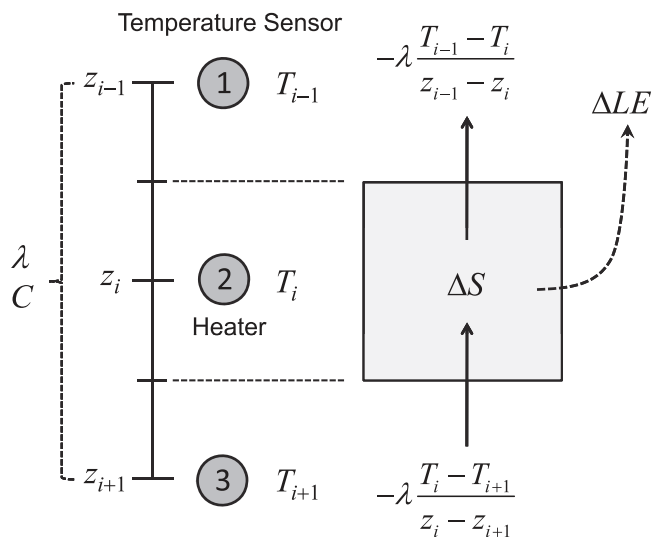
Figure 1. A schematic diagram of the heat balance method used with a tri-needle heat pulse probe after *Heitman et al.* [2008b].

interval shown in Figure 1 [*Heitman et al.*, 2008a, 2008b]. Using the measured soil temperatures at the three depths (T_1, T_2, and T_3) coupled with the calculated λ, conductive heat fluxes for the two depths are calculated (first term on the right-hand side in equation (1)). The change of sensible heat storage, ΔS (equation (2)), and latent heat of vaporization, L, are calculated using the measured soil temperature at T_2. Finally the subsurface evaporation rate, E, between $z_{i-1/2}$ and $z_{i+1/2}$ is calculated from equation (1). We refer to determined E using the *Heitman et al.* [2008a, 2008b] method for as the subsurface evaporation rate from heat balance (SE$_{HB}$) method to make a clear distinction from E determined with the subsurface evaporation rate from a water balance (SE$_{WB}$) approach, defined later.

2.2. Numerical Simulations

[9] Different surface boundary conditions were applied to numerically simulate vertical profiles for soil temperature and water content changes during evaporation. First, evaporation from a 15 cm long soil column under a simple constant atmospheric condition was simulated to detect limitations of the heat balance method. Second, evaporation from a 20 cm long soil column under diurnally varied atmospheric conditions was simulated to test the applicability of the heat balance method for field measurements. The following governing flow equations and initial and boundary conditions for water and heat transport were used for simulating nonisothermal liquid water, water vapor, and heat flow.

2.2.1. Governing Flow Equations

[10] The one-dimensional conservation of water equation including both liquid water and water vapor for nonisothermal conditions in a variably saturated soil is given as [*Philip and de Vries*, 1957; *Saito et al.*, 2006]:

$$\frac{\partial(\theta_w + \theta_v)}{\partial t} = -\frac{\partial(q_w + q_v)}{\partial z}$$
$$= \frac{\partial}{\partial z}\left[K_{Lh}\left(\frac{\partial h}{\partial z} + 1\right) + K_{LT}\frac{\partial T}{\partial z} + K_{vh}\frac{\partial h}{\partial z} + K_{vT}\frac{\partial T}{\partial z}\right],$$

(3)

where θ_w is volumetric liquid water content (m^3 m^{-3}), θ_v is volumetric water vapor content (expressed as an equivalent water content, $= \theta_{air} \times \rho_v/\rho_w$, m^3 m^{-3}), θ_{air} is volumetric air content (m^3 m^{-3}), ρ_v and ρ_w are densities of water vapor and liquid water (kg m^{-3}), q_w and q_v are the flux densities of liquid water and water vapor (expressed as an equivalent water flux density, m s^{-1}), h is the soil water pressure head (m), K_{Lh} (m s^{-1}) and K_{LT} (m^2 $^{\circ}$C^{-1} s^{-1}) are the isothermal and thermal hydraulic conductivities for liquid water fluxes, respectively, and K_{vh} (m s^{-1}) and K_{vT} (m^2 $^{\circ}$C^{-1} s^{-1}) are the isothermal and thermal vapor hydraulic conductivities, respectively. The expressions for hydraulic conductivities are detailed in Table 1.

[11] The principle of heat conservation is given as [*de Vries*, 1958]:

$$\frac{\partial S_h}{\partial t} = -\frac{\partial q_h}{\partial z},$$

(4)

where S_h is soil heat storage (J m^{-3}), and q_h is the soil heat flux density (J m^{-2} s^{-1}). The total soil heat flux density, q_h,

is defined as the sum of (1) conduction of sensible heat; (2) sensible heat by convection of liquid water and (3) water vapor; and (4) latent heat of vapor flow [*de Vries*, 1958]:

$$q_h = -\lambda\frac{\partial T}{\partial z} + C_w(T - T_r)q_w + C_v(T - T_r)q_v + Lq_v,$$

(5)

where T_r is an arbitrary reference temperature ($^{\circ}$C), and C_w and C_v are volumetric heat capacities of liquid water ($=4.18$ MJ m^{-3} $^{\circ}$C^{-1}) and water vapor ($=1.8$ MJ m^{-3} $^{\circ}$C^{-1}), respectively. The soil heat storage, S_h, is defined as the sum of sensible and latent heat:

$$S_h = C_s(T - T_r)\theta_s + C_w(T - T_r)\theta_w + C_v(T - T_r)\theta_v + L\theta_v$$
$$= (C_s\theta_s + C_w\theta_w + C_v\theta_v)(T - T_r) + L\theta_v = C(T - T_r) + L\theta_v,$$

(6)

where C_s is the volumetric heat capacity of the solid phase ($=1.92$ MJ m^{-3} $^{\circ}$C^{-1}), and θ_s is volumetric fraction of the solid phase (m^3 m^{-3}). In equations (5) and (6), local thermal equilibrium between the solid, liquid, and water vapor phases is assumed.

2.2.2. Initial and Boundary Conditions

[12] Initial conditions for the water and heat flow equations are given by

$$h(z, 0) = h_i(z)$$

(7)

$$T(z, 0) = T_i(z),$$

(8)

where $h_i(z)$ and $T_i(z)$ are initial soil water pressure head and soil temperature, respectively.

[13] Soil surface heat flux and evaporation rate were determined from the partition of the energy balance and were applied as surface boundary conditions for the water and heat flow equations [e.g., *Saito et al.*, 2006]:

$$q_w(0, t) + q_v(0, t) = E_{sf}$$

(9)

$$\left[-\lambda\frac{\partial T}{\partial z} + C_w(T - T_r)(q_L + q_v) + Lq_v\right]\bigg|_{z=0}$$
$$= -G = -R_n + H_s + LE_{sf},$$

(10)

where E_{sf} is the surface evaporation rate (m s^{-1}), G is the surface heat flux density (W m^{-2}), R_n is the net radiation (W m^{-2}), and H_s is the sensible heat flux density (W m^{-2}). While R_n and G are positive downward, H_s and LE_{sf} are positive upward. The soil surface evaporation can be calculated from the difference between the water vapor densities of the air, ρ_{va} (kg m^{-3}), and the soil surface, ρ_{vs} (kg m^{-3}):

$$E_{sf} = \frac{\rho_{vs} - \rho_{va}}{\rho_w \cdot r_a} = \frac{\text{RH}_{sf}\rho_{sv} - \text{RH}_{air}\rho_{sv}}{\rho_w \cdot r_a},$$

(11)

where ρ_w is the density of liquid water (kg m^{-3}, see Table 1), r_a is the aerodynamic resistance to water vapor flow and heat transfer (s m^{-1}), RH$_{sf}$ and RH$_{air}$ are the relative humidity (-) at the soil surface (Table 1) and the air, respectively, and ρ_{sv} is the saturation vapor density (kg m^{-3}, Table 1). The sensible heat flux, H_s, can be defined as [*van Bavel and Hillel*, 1976]:

Table 1. Hydraulic Conductivities (K) for Liquid (L) and Vapor (v) Water-Flux Accounting for Isothermal (h) and Thermal (T) Conditions

Hydraulic Conductivity	Parameter	Constant/Equation[a]
$K_{Lh} = K_s S_e^{\,l} \left(\int_0^{S_e} \frac{dS_e}{|h|} \Big/ \int_0^1 \frac{dS_e}{|h|} \right)^2$	l = Pore connectivity coefficient	0.5
$K_{LT} = K_{Lh} \left(h G_{wT} \frac{1}{\gamma_0} \frac{d\gamma}{dT} \right)$	G_{wT} = Gain factor	7
	γ = Surface tension of soil water, g s^{-2}	$75.6 - 0.1425\,T - 2.38 \times 10^{-4}\,T^2$
	γ_0 = Surface tension at 25 °C, g s^{-2}	71.89
	D = Vapor diffusivity in soil, m^2 s^{-1}	$\tau_a \theta_{air} D_a$
	τ_a = Tortuosity factor in gaseous phase	$\theta_{air}^{7/3}/\theta_{sat}^2$
$K_{vh} = \frac{D}{\rho_w} \rho_{sv} \frac{Mg}{RT_{abs}} \mathrm{RH}_{sf}$	D_a = Vapor diffusivity in air, m^2 s^{-1}	$2.12 \times 10^{-5}\,(T_{abs}/273.15)^2$
	ρ_w = Density of liquid water, kg m^{-3}	$1000 - 7.37 \times 10^{-3}\,(T-4)^2 + 3.79 \times 10^{-5}\,(T-4)^3$
	ρ_{sv} = Saturation vapor density, kg m^{-3}	$\exp(31.37 - 6014.79/T_{abs} - 7.92 \times 10^{-3}\,T_{abs})/T_{abs} \times 10^{-3}$
	RH_{sf} = Relative humidity of soil surface	$\exp(h\,M\,g/R\,T_{abs})$
	M = Molecular weight of water, kg mol^{-1}	0.018015
	g = Gravitation acceleration, m s^{-2}	9.81
	R = Universal gas constant, J mol^{-1} K^{-1}	8.341
$K_{vT} = \frac{D}{\rho_w} \eta \mathrm{RH}_{sf} \frac{d\rho_{sv}}{dT}$	η = Enhancement factor	$\eta = 9.5 + 3\theta_w/\theta_{sat} - 8.5 \exp\left\{-[(1 + 2.6/\sqrt{f_c})\theta_w/\theta_{sat}]^4\right\}$
	f_c = mass fraction of clay (f_c)	0.02

[a]K_s, saturated hydraulic conductivity; S_e, effective liquid saturation; T, temperature in Celsius; T_{abs}, absolute temperature; h, pressure head; θ_w, volumetric water content; θ_{sat}, saturated water content; θ_{air}, volumetric air content.

$$H_s = C_a \frac{T_s - T_a}{r_a}, \qquad (12)$$

where C_a is the volumetric heat capacity of air ($=1200$ J m^{-3} °C^{-1}), and T_s and T_a are temperature (°C) of the soil surface and the air, respectively.

2.2.2.1. Simulation Under Constant Atmospheric Conditions

[14] To simulate evaporation from the 15 cm long soil column, constant atmospheric conditions and simplified parameters were employed throughout the simulated time period of 30 days. Although R_n has a large impact on accelerating the evaporation rates [Penman, 1941; Fritton et al., 1970], we simulated a laboratory evaporation experiment in a chamber with no heater lamps enhancing the evaporation rate. With this in mind, R_n was assumed to be 0, T_a was 25 °C, and RH$_{air}$ was assumed to equal 0.20 (20%). Although r_a is a function of wind speed, air- and soil-temperatures [Camillo and Gurney, 1986], a constant value of 200 s m^{-1}, which corresponds to an approximate wind speed of 1.7 m s^{-1} [Jensen et al., 1990], was assumed. The values of r_a and RH$_{air}$ were chosen so that evaporation rate at stage 1 would be around 0.4 cm d^{-1} (shown in section 3.1.1).

[15] Zero water flux and a constant temperature equal to 25 °C were applied as the lower boundary conditions for the column, written here as:

$$q_w(-15, t) + q_v(-15, t) = 0 \qquad (13)$$

$$T(-15, t) = 25. \qquad (14)$$

[16] Initial conditions for the saturated soil column included hydrostatic equilibrium with -15 cm pressure head at the top of the soil column (0 cm at bottom, $h_i(z) = -z-15$), and the initial temperature was assumed constant at 25 °C ($T_i(z) = 25$).

2.2.2.2. Simulation Under Diurnal Atmospheric Conditions

[17] In order to simulate evaporation under field-like conditions, diurnally varying air temperature, T_a; relative humidity of the air, RH$_{air}$; and solar radiation, R_s, were employed. The air temperature and relative humidity were determined by trigonometric cosine functions as follows [Kirkham and Powers, 1972];

$$T_a = \frac{T_{\max} + T_{\min}}{2} + \frac{T_{\max} - T_{\min}}{2} \cdot \cos\left[2\pi\left(\frac{t - 13}{24}\right)\right] \qquad (15)$$

$$\mathrm{RH}_{air} = \overline{\mathrm{RH}} + \frac{\mathrm{RH}_{\max} - \mathrm{RH}_{\min}}{2} \cdot \cos\left[2\pi\left(\frac{t - 1}{24}\right)\right], \qquad (16)$$

where $T_{\max}$ and $T_{\min}$ are the maximum and minimum air temperatures, respectively, and $\overline{\mathrm{RH}}$, RH$_{\max}$, and RH$_{\min}$ are the average, maximum, and minimum air relative humidities, respectively. Assuming that the atmospheric actual vapor pressure is constant during the day, RH$_{\max}$ and RH$_{\min}$ can be determined from given $T_{\max}$, $T_{\min}$, and $\overline{\mathrm{RH}}$ values. A value of the incoming shortwave solar radiation, R_s, at any given time can be calculated based on the work of Campell [1985].

$$R_s = f \cdot \max\left\{R_s^d[\sin\varphi\sin\delta + \cos\varphi\cos\delta\cos 2\pi(t - 12)/24], 0\right\}. \qquad (17)$$

where $R_s{}^d$ is the daily solar radiation (W m^{-2}), φ (rad) is the site latitude, and δ is the solar declination (rad). A factor, f, is used to adjust the daily summation of R_s equal to $R_s{}^d$. Net radiation is determined by

$$R_n = (1 - \alpha)R_s + \sigma\varepsilon_s\left(\varepsilon_a T_a^4 - T_s^4\right), \qquad (18)$$

where α is the soil albedo, σ is the Stefan–Boltzmann constant, and ε_s and ε_a are the emissivity of soil and atmosphere, respectively. Although the aerodynamic resistance to water vapor flow and heat transfer, r_a, is assumed as a constant value in simulations with constant atmospheric conditions, it was calculated by an iterative procedure proposed by [Camillo and Gurney, 1986] as follows;

$$r_a = \frac{1}{U_z k^2}\left[\ln\left(\frac{z_m - d + z_{om}}{z_{om}}\right) + \psi_m\right]\left[\ln\left(\frac{z_h - d + z_{oh}}{z_{oh}}\right) + \psi_h\right],$$

(19)

where U_z is wind speed (m s^{-1}), k is the von Karman constant, d is the zero plane displacement (m), z_m and z_h are the height of wind speed and temperature measurement (m), respectively, z_{om} and z_{oh} are the surface roughness length for momentum flux and heat flux (m), respectively, and ψ_m and ψ_h are the atmospheric stability correction factors for momentum flux and heat flux (-), respectively. In this study, we used $T_{\max} = 30$ °C, $T_{\min} = 20$ °C, $\overline{\mathrm{RH}} = 0.6$ (60%), $U_z = 3$ m s^{-1}, and $R_s{}^d = 180$ (W m^{-2}) for all 20 simulation days. Figure 2 shows the diurnal variations of T_a, RH$_{air}$, and R_s. T_a has the maximum (30 °C) and minimum values (20 °C) at 1 pm and 1 am, respectively, while RH$_{air}$ has the maximum (0.77) and minimum values (0.43) at 1 am and 1 pm, respectively. R_s shows the peak of 718 W m^{-2} at noon.

[18] Zero gradients of pressure head and temperature were applied as the lower boundary conditions.

$$dh/dz = 0$$

(20)

$$dT/dz = 0,$$

(21)

and uniform pressure head of -100 cm ($h_i(z) = -100$) and soil temperature of 20 °C ($T_i(z) = 20$) were given as initial conditions.

2.2.3. Soil Hydraulic Properties and Thermal Conductivities

[19] In the simulations, three arbitrarily chosen soils with different textures were used. We also assumed the nonisothermal water flow equation proposed by *Philip and de Vries* [1957] and heat transport equation proposed by *de Vries* [1958] are applicable in these soils. Three different soil textures (i.e., sand, silt, and silty clay) from the database of *Carsel and Parrish* [1988] were used for numerical simulations of soil water evaporation. Although Carsel and Parrish focused on the Mualem–van Genuchten [*van Genuchten*, 1980] parametric model, the residual water content in this model is an empirical parameter and it is unrealistic that water content reduction stops at the residual water content in the case of evaporation. It was found that this model leads to numerical simulation instabilities and underestimates the unsaturated hydraulic conductivity for dry regions close to the residual water contents [*Sakai et al.*, 2009]. Because the water content for coarse textured soils approaches its residual value already at relatively high pressure heads, the soil water retention–pressure head relationship proposed by *Fayer and Simmons* [1995] was used for sand and silt.

$$\theta_w = \chi\theta_a + (\theta_{sat} - \chi\theta_a)[1 + (-\alpha h)^n]^{-(1 - 1/n)},$$

(22)

where θ_{sat} is the saturated water content (m^3 m^{-3}), and α (m^{-1}), n, and θ_a (m^3 m^{-3}) are empirical shape parameters. The parameter χ is described as $1 - \ln(-h)/\ln(-h_m)$, where h_m is the pressure head at the water content equal to 0 (i.e., $= -10^7$ cm). The van Genuchten model parameterized with values from *Carsel and Parrish* [1988] was used for silty clay:

$$\theta_w = \theta_r + (\theta_{sat} - \theta_r)[1 + (-\alpha h)^n]^{-(1 - 1/n)},$$

(23)

where θ_r is the residual water content (m^3 m^{-3}). The unsaturated hydraulic conductivity was estimated with *Mualem*'s [1976] pore size distribution model for both retention functions. The parameters employed for each of the soils are shown in Table 2, and Figure 3 illustrates the modeled soil water retention (Figure 3a) and hydraulic conductivity curves (Figure 3b).

[20] The *Chung and Horton* [1987] model was used to describe the water content–dependent thermal conductivity:

$$\lambda = b_1 + b_2\theta_w + b_3\theta_w{}^{0.5},$$

(24)

where b_1, b_2, and b_3 are empirical parameters (W m^{-1} °C^{-1}). The parameters for sand, loam, and clay used in *Chung and Horton* [1987] were used for sand, silt, and silty clay, respectively (Table 2). All three soil textures were used in simulations under constant atmospheric conditions, while only silt was used for simulation under diurnal atmospheric cycles.

[21] Governing equations (3) and (4) describing coupled movement of liquid water, heat, and water vapor were solved using the HYDRUS-1D code [*Šimůnek et al.*, 2008]. Since mesh densities affect the results of this coupled transport simulation [*Novak*, 2010], a maximum density was found that minimized numerical oscillations and differences in results when compared with different mesh-sized simulations. The 15 cm long soil profile for simulation with constant atmospheric conditions was divided into 300 elements, with thicknesses that increased linearly from 0.00099 cm at the surface to 0.099 cm at the bottom. The 20 cm long soil profile (i.e., diurnal atmospheric boundary simulation) was divided into 400 elements, with thicknesses of 0.00099 cm
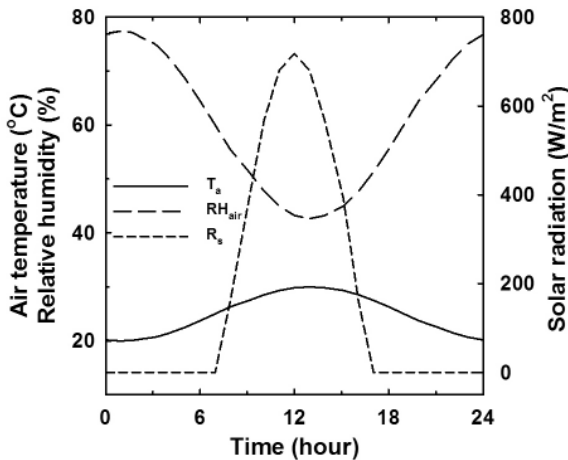
Figure 2. Diurnal variations of air temperature (T_a, solid line), relative humidity of air (RH$_{air}$, long dashed line), and solar radiation (R_s, short dashed line) used in the simulation.

Table 2. Hydraulic Property and Thermal Conductivity Parameters Used in Numerical Simulations

Sample	Hydraulic Property					Thermal Conductivity		
	$\theta_r\ (\theta_a)$	θ_{sat}	α (cm^{-1})	n	K_s (cm d^{-1})	b_1 (W m^{-1} °C^{-1})	b_2 (W m^{-1} °C^{-1})	b_3 (W m^{-1} °C^{-1})
Sand	0.0625	0.43	0.147	2.73	712.8	0.228	−2.406	4.909
Silt	0.16	0.46	0.0167	1.48	6	0.243	0.393	1.534
Silty Clay	0.07	0.36	0.005	1.09	0.48	−0.197	−0.962	2.521

at the top increasing to 0.099 cm at the bottom. The time step was allowed to vary between the initial and maximum time steps of 1×10^{-8} and 0.01 day, respectively. Soil temperatures and water contents for each discretized node were output in 0.01 day ($\approx$15 min) time intervals. Simulated soil temperatures were output with a resolution of 0.001 °C to be consistent with the output resolution of thermistors used in heat-pulse probes. Simulated temperatures of three depths, thermal conductivity (equation (24)), and heat capacity of soil (equation (6)) based on simulated water contents were used to calculate subsurface evaporation rates from equation (1). In order to evaluate the impact of three different observation grids of 6, 3, and 1 mm on subsurface evaporation rate estimation, water contents and temperatures for every 1 mm of depth were derived by linearly interpolating the simulated results at two neighboring finite element nodes after simulation. Thermal water vapor flux induced by a heat pulse from the HPP measurement was studied in detail previously and is small except when using larger heater needles (i.e., $\geq$ 4 mm) or larger pulse intensity (i.e., $\geq$ 600 W m^{-1}) as shown by *Saito et al.*, [2007]. To focus on estimation of evaporation rates from heat balance, the heat-pulse stage was not simulated in this study.

2.2.4. Subsurface Evaporation Rate Calculation From Water Balance

[22] While the model suggested by *Heitman et al.* [2008a, 2008b] is based on heat balance considerations (equation (1)), subsurface evaporation rates may be also calculated with a water balance approach using numerical simulations to compute volumetric water vapor contents and water vapor fluxes. A mass conservation equation that accounts for water vapor content is given as [*Nassar et al.*, 1992]:

$$\frac{\partial \theta_v}{\partial t} = -\frac{\partial q_v}{\partial z} + e \,, \tag{25}$$

where e is a depth-dependent evaporation rate with units of 1 s^{-1} ($E = e\, dz$, cm s^{-1}). The evaporation rate at each internal node can be calculated with a discretized form of equation (25) [*Sakai et al.*, 2009]:

$$E_i^j = \left(\theta_{vi}^j - \theta_{vi}^{j-1} \right) \frac{dz}{dt} + \left(q_{vi+1/2}^{j-1/2} - q_{vi-1/2}^{j-1/2} \right). \tag{26}$$

[23] We now define this subsurface evaporation rate, E_i^j, determined by equation (26) as the subsurface evaporation rate from a water balance (SE$_{WB}$) to distinguish from the heat balance method (equation (1)), SE$_{HB}$. Since the error in water mass balance from HYDRUS simulations was extremely small, directly estimated SE$_{WB}$ values provide an accurate reference to test indirectly estimated SE$_{HB}$ values.

3. Results and Discussions

[24] Below we discuss results from numerical HYDRUS-1D simulations, which allow a theoretical assessment of the heat balance method and illustrates some limitations of this approach. We apply the heat balance method for subsurface evaporation assessment using numerical data at different spacings to examine the tradeoff between
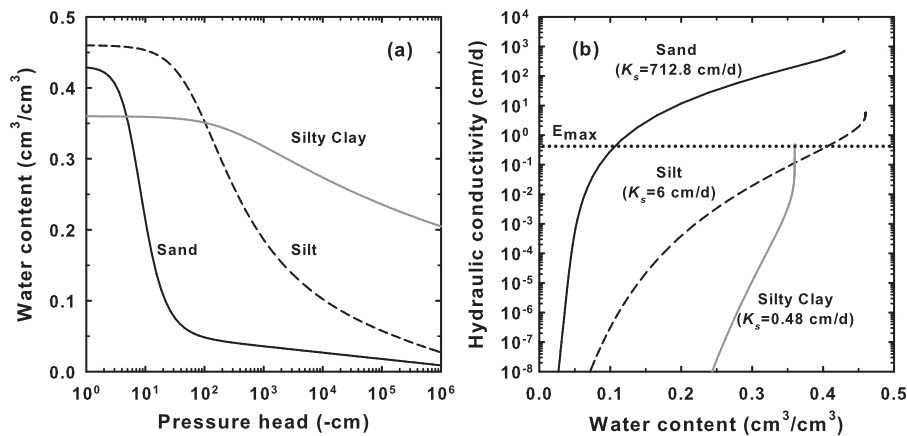
Figure 3. (a) The soil water retention curves and (b) soil hydraulic conductivities modeled for the numerical experiments. We point to E$_{max}$, which represents the potential evaporation rate for stage 1 and is given for comparison to the hydraulic conductivities near saturation.

maximizing accuracy and minimizing the required number of HPP thermistors. Physical challenges associated with application of the heat balance method related to the probe geometry and needle configuration are also discussed.

3.1. Evaporation Simulations With Constant Boundary Condition

3.1.1. Simulated Results of Coupled Water and Heat Transport

[25] Water flow and heat transport were simulated with HYDRUS-1D to quantify the soil water evaporation process. Figures 4a, 4b, and 4c show simulated individual liquid- (LPF, $q_w(0, t)$) and vapor-phase fluxes (VPF, $q_v(0, t)$) as well as total flux (LPF+VPF, E_{sf}) at the soil surface. The LPF is here defined as the liquid water flow within the soil

arriving at and evaporating from its surface into the atmosphere [*Novak*, 2010]. Figures 4d, 4e and 4f show soil profile temperature changes for sand, silt, and silty clay. Results obtained for sand (Figure 4a) and silt (Figure 4b) clearly distinguish stage 1 and stage 2 evaporation processes. A mean stage 1 evaporation rate of 0.4 cm d^{-1} was maintained for 5.7 days for sand; and 0.43 cm d^{-1} was maintained for silt over 6.2 days. Thereafter evaporation rates decreased. The liquid-phase flux was dominating during stage 1, while the vapor-phase flux dominated stage 2 evaporation as shown in Figures 4a and 4b [*Yamanaka and Yonetani*, 1999]. The initially large evaporation rates near 0.43 cm d^{-1} found in sand and silt simulations during stage 1 evaporation were sustained by relatively high hydraulic conductivities characteristic of these soil textures (i.e., see
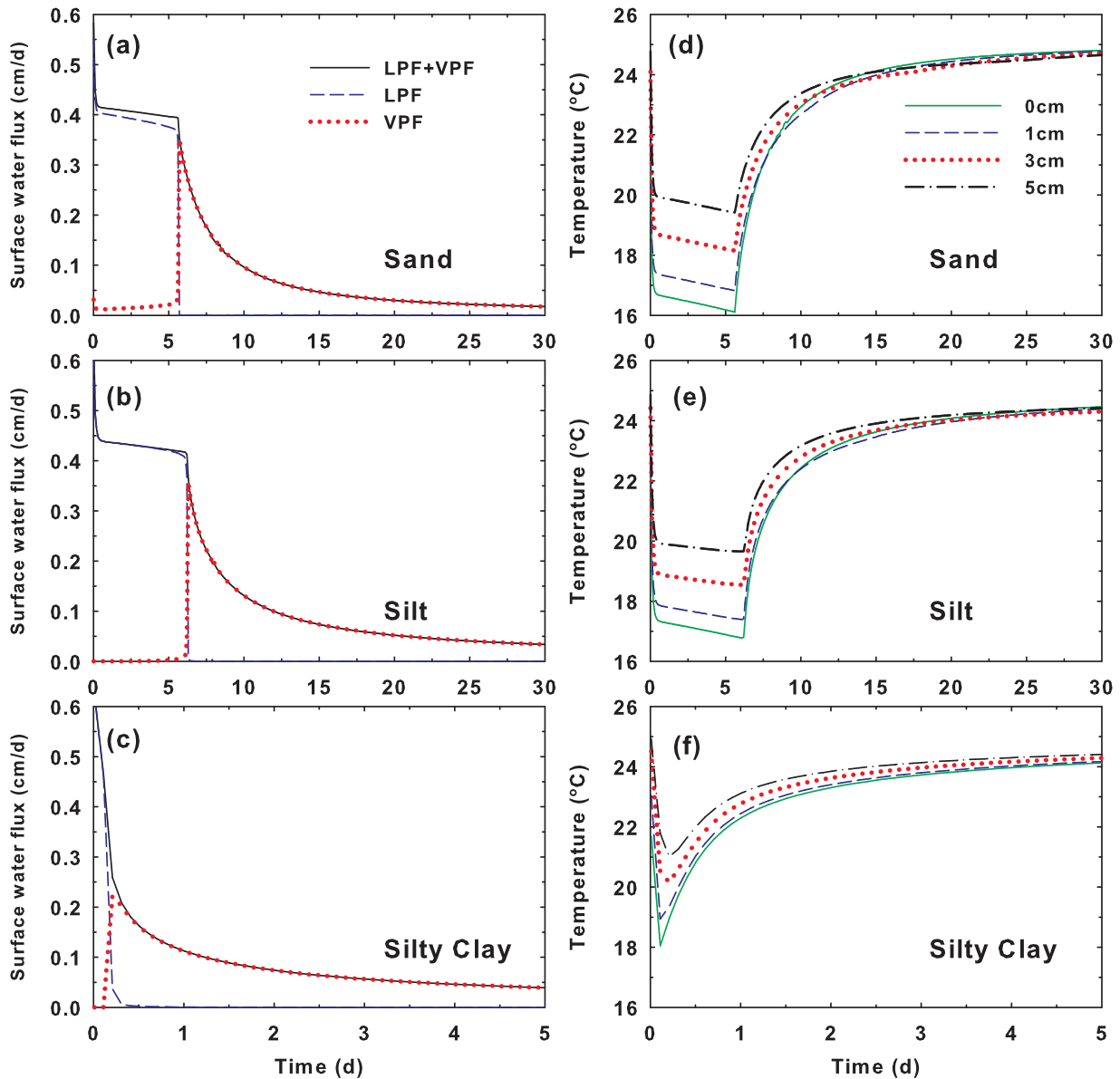
Figure 4. (a–c) Simulated soil surface water fluxes with components of liquid- (LPF) and vapor-phase fluxes (VPF) for sand, silt, and silty clay textures, respectively. (d–f) Soil temperature changes given for sand, silt, and silty clay textures, respectively. Note Figures 4c and 4f are plotted at 1/6 the temporal scale for emphasis of the early conditions.

Figure 3b). In contrast to sand and silt textures, stage 1 evaporation was not maintained for the silty clay (Figure 4c) because its saturated hydraulic conductivity was an order of magnitude less and about equal to the potential evaporation rate shown in Figure 4b. The silty clay evaporation process exhibited rapid transition to stage 2 and was therefore only plotted for 5 days in Figures 4c and 4f. The low hydraulic conductivity of silty clay coupled with a relatively small matric potential gradient limited the rate of water supply to the soil surface, which yielded a stage 1 evaporation rate that was lower than the potential evaporation rate determined by atmospheric demand [*Jury and Horton*, 2004].

[26] The simulated soil temperature in sand (Figure 4d) and silt (Figure 4e) exhibited similar trends where temperatures quickly decreased from 25 °C (initial value) to values between 17.5 and 21 °C, thereafter decreasing gradually throughout stage 1 evaporation. The transition to stage 2 evaporation was accompanied by a rapid increase in soil temperature that gradually diminished as it approached the 25 °C boundary temperature. This temperature change trend during stage 1 and stage 2 evaporation was also demonstrated in laboratory measurements by *Qiu and Ben-Asher* [2010]. The expected maximum temperature decrease at the soil surface caused by heat loss from the latent heat of vaporization reduced temperatures to around 16 °C for sand and to 17 °C for silt during stage 1. This large drop in soil surface temperature reduced the soil surface vapor density, resulting in an approximate 45% reduction of the initially computed evaporation rate of 0.79 cm d^{-1} (equation (11)). Under the 25 °C isothermal boundary conditions imposed in the simulation, the energy transition from stage 1 to stage 2 is remarkably clear in Figure 4. As the evaporation front moved below ground, latent heat depletion was efficiently reduced by the insulating drier soil layer between the drying front and soil surface. Temperatures in the silty clay simulation exhibit no stage 1 evaporation process but also decreased from 25 to 18 °C during the first few hours and then showed the gradual increase back to the boundary condition temperature of 25 °C.

[27] Figure 5 shows temporal snapshots of the upper 5 cm profile of simulated subsurface evaporation rate (determined by water balance, equation (26)), soil temperature, water content, and thermal conductivity (equation (24)) on days 5, 6.2, 10, 20, and 30 for the silt simulation. Note that day 6.2 was the transition time between stage 1 and stage 2 evaporation, discussed in section 3.1.4. Short time profiles of evaporation rate as well as temperature overlapped on days 5 and 6.2 where stage 1 evaporation was ongoing (i.e., not seen in Figure 5a). Temperature profiles increased linearly with depth and the water content profile was relatively uniform during stage 1 (Figures 5b and 5c). During stage 2 (days 10, 20, and 30), soil water evaporation occurred across a relatively narrow soil profile showing a normally distributed rate around the peak value (Figure 5a), where the distribution of the evaporation front spread and diminished in magnitude as it retreated deeper into the soil. Considering the temperature profile, each of the peak rates shown in Figure 5a have corresponding inflections in the temperature profiles shown in Figure 5b, which result from maximum cooling at the drying front. At the three depths shown, water content profiles (Figure

5c) exhibit a dramatic transition that is directly associated with the diminishing water content at the drying front. Just above the drying front the soil water content is approaching the residual water content (i.e., $\theta_w \leq 0.03$ cm^3 cm^{-3}) and water vapor is the dominant form of transport to the surface [*Yamanaka and Yonetani*, 1999]. This reduction of water content at the drying front had a commensurate effect on thermal conductivity (Figure 5d). In the following the heat balance method (equation (1)) is employed to independently compute subsurface evaporation based on these simulated soil profiles of temperature, water content, and thermal conductivity.

3.1.2. Location of Soil Water Vaporization

[28] Subsurface evaporation was computed using a water balance (SE$_{WB}$, equation (26)) in order to plot the descending depth-dependent evaporation front between the soil surface and a 4 mm depth (Figure 6). Subsurface evaporation calculations begin at the first subsurface node 0.00099 cm below the surface, therefore, liquid-phase water fluxes at the soil surface are plotted in Figure 6 as evaporation rates at the surface (LPF in Figure 4). We distinguish between liquid water vaporized at the soil surface, referred to as "surface evaporation" and liquid water vaporized in the subsurface, referred to as "subsurface evaporation." We also acknowledge a combination of these two processes can occur and refer to it as "transient evaporation," which occurred on day 1 in sand and day 6.3 in silt (Figures 6a and 6b). In this case the transient evaporation from the soil surface came from both liquid- and vapor-phase components illustrated in Figures 4a and 4b. The surface evaporation rate contribution was 0.41 cm d^{-1} with an additional 0.01 cm d^{-1} contributed from vapor phase flux in sand (Figure 4a), which occurred between the surface and the first mesh node at 0.00099 cm. Subsurface evaporation in sand started from day 6, and the recession of the drying front downward was faster than in the finer textured soils (the peak was 0.11 cm at 6.3 days and 0.33 cm at 7.5 days). In the transient and subsurface evaporation stage, water vaporization occurred over depths ("evaporation region") of up to 0.07 cm. By comparison, *Novak* [2010] showed a simulated subsurface evaporation zone with a width of 0.02−0.07 cm, which is consistent with our result.

[29] During day 1 in silt (Figure 6b), only surface evaporation occurred at a rate of 0.44 cm d^{-1}, while there was no subsurface evaporation below a 0.00099 cm depth. This is consistent with all cases where only surface water flux was taking place as liquid-phase (i.e., no vapor-phase flow, Figure 4b). Meanwhile, on day 7.5 in silt, all of the water vaporization occurred within the subsurface with the peak being 0.1 cm d^{-1} at the 0.18 cm depth. In this case the vapor-phase flow was the dominant source for soil water flux emitted at the surface (Figure 4b). During day 6.3 in silt a transient evaporation stage occurred, exhibiting both surface evaporation (0.02 cm d^{-1}) and subsurface evaporation (peak of 0.13 cm d^{-1} at 0.02 cm depth). In the case of silty clay (Figure 6c) an extremely short surface evaporation stage was followed by a lengthy transition stage extending to nearly 0.5 days. In the subsurface evaporation stage beyond 0.5 days, the evaporation rates were smaller than for coarser textures and the recession of the evaporation region occurred at a slower rate (0.025 cm descent between 6.3 and 7.5 days).
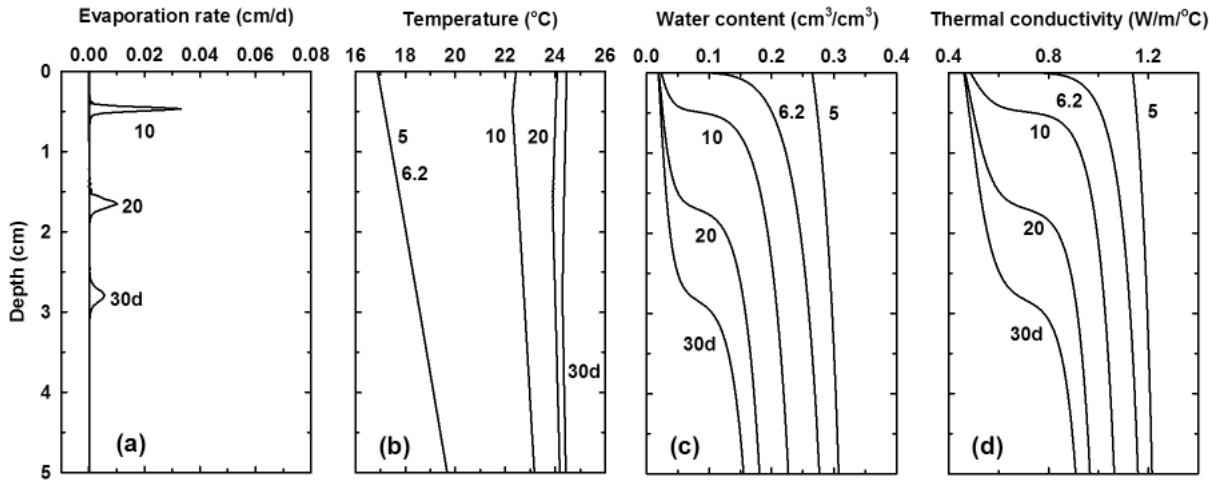
Figure 5. Simulated silt texture profiles at 5, 6.2, 10, 20, and 30 days showing (a) evaporation rates based on water balance (SE$_{WB}$, equation (26)), (b) soil temperatures, (c) water contents, and (d) thermal conductivity. Note that the temperature profile at 6.2 days overlaps that of the 5 day profile.

3.1.3. Local and Total Subsurface Evaporation Rates

[30] Results from the simulated subsurface evaporation process were used to test the heat balance method based on equation (1). One of the major objectives was to investigate the impact of temperature observation grid spacing on the resulting subsurface evaporation calculations. Three different spacings were considered; 6 mm spacing corresponding to the tri-needle HPP [*Heitman et al.*, 2008a, 2008b], 3 mm spacing corresponding to the penta-needle HPP [*Yang and Jones*, 2009], and 1 mm temperature observation grid spacing. The soil thermal conductivity, λ, and volumetric heat capacity of moist soil, C, used in equations (1) and (2) were computed from equations (6) and (24). Average values of λ and C between the top and bottom temperature sensors were obtained from HPP measurements (Figure 1). To be consistent with this HPP measurement, λ and C values in this numerical study were calculated from averaged water content between the top and bottom temperature observation grids. Figure 7a shows temporal changes in calculated local subsurface evaporation rates, SE$_{HB}$, for each
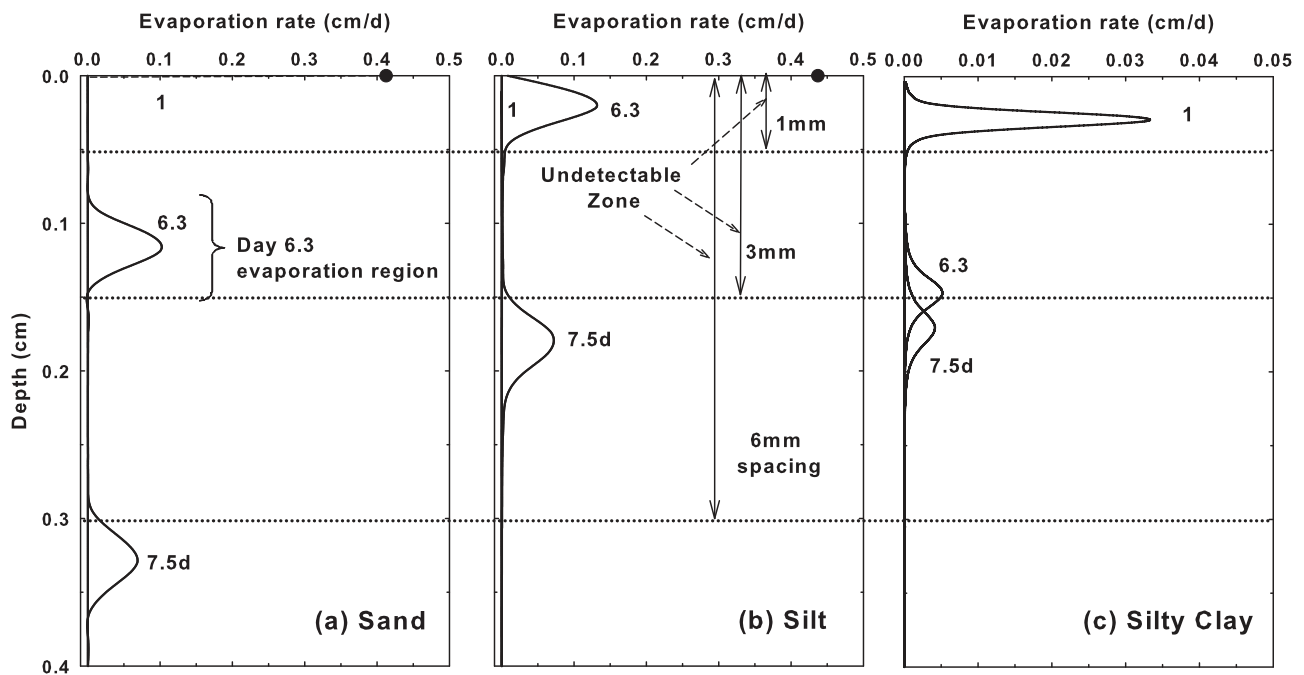

Figure 6. Simulated evaporation rate profiles for (a) sand, (b) silt, and (c) silty clay based on a water balance (SE$_{WB}$ equation (26)) at 1, 6.3, and 7.5 days. Dotted lines represent the undetectable zones (half grid spacing) of the heat balance method with 1, 3, and 6 mm temperature measurement spacing. Note Figure 6c is plotted at 1/10 the *x* axis scale for clarity and dots at the surface in Figures 6a and 6b are LPF values indicating water vaporization at the surface.

soil depth increment defined by a 3 mm temperature observation grid for silt (i.e., $1.5-4.5$, $4.5-7.5$, $7.5-10.5$ mm). To calculate SE_{HB} in the $1.5-4.5$ mm depth, temperatures at 0, 3, and 6 mm depths were used in equation (1) and 0.1 days (≈15 min) was used as the observation time interval, $t^j - t^{j-1}$, in equation (2). Here averaged water contents between a 0 and 6 mm depth were used to calculate λ and C. Each 3 mm soil depth increment exhibited a peak rate of evaporation in descending order. In the $1.5-4.5$ mm region, soil water evaporation started on day 6 achieving a maximum SE_{HB} calculation of 0.16 cm d^{-1} on day 8 and diminished to near zero by day 12. This suggests soil water evaporation took place at the soil surface and possibly down to 1.5 mm depth before day 6 of the simulation. The general trend is for the shallower depths to exhibit larger peaks at earlier times and for the deeper depths to exhibit smaller peaks at later times (i.e., 0.04 cm d^{-1} at day 21 for the $16.5-19.5$ mm depth). This trend was consistent with the field measurements of *Heitman et al.* [2008b] showing larger peaks in the upper layer ($3-9$ mm depths) at earlier times and in the lower layer ($9-15$ mm depths) at later times. As the drying front went deeper with time, the evaporation rates diminished by a factor of 4 over 20 days, which was consistent with the simulated subsurface evaporation rates determined from water balance (SE_{WB}, Figure 5a). The overlapping of SE_{HB} for each increment demonstrates that evaporation occurred not from a plane but from a soil layer of finite width [*Heitman et al.*, 2008b]. The total subsurface evaporation rate from heat balance (TSE_{HB}) during the evaporation simulation was determined by summing up all the calculated SE_{HB} from 1.5 mm to the 100 mm depth. The total subsurface evaporation rates from water balance (TSE_{WB}) below 1.5 mm depth was also plotted in Figure 7 to compare with TSE_{HB}, which exhibited negative values from the beginning of the simulation up to day 6. Although negative evaporation rate values can suggest subsurface condensation [*Heitman et al.*, 2008a; *Sakai et al.*, 2009], water vapor condensation could not happen in this simulation with a constant atmospheric boundary because the TSE_{WB} exhibited no negative values. Furthermore, TSE_{HB} underestimated the resulting TSE_{WB} until day 20. This indicates that calculating the subsurface evaporation using equation (1) contains some systematic errors.

3.1.4. Improvement of Subsurface Evaporation Estimation

[31] To investigate the underestimation of the SE_{HB}, we focused on the calculation in the $1.5-4.5$ mm soil layer at day 6.2 when a large underestimation was observed just before subsurface evaporation in this soil layer started to increase (Figure 7a). The large water content gradient illustrated in Figure 5c is associated with evaporation on day 6.2 and since thermal conductivity is water content–dependent, the λ profile also shows a large gradient at the drying front (Figure 5d). At this same time, soil temperature was minimal at the surface and conductive heat flux was upward throughout the profile (Figure 5b).

[32] To illustrate the importance of accurately estimating λ, especially near the drying front, we plot the spatial and temporal variation in estimated evaporation rates using both locally determined (Figure 7b) versus averaged thermal conductivity (Figure 7a). When averaging λ across the $0-6$ mm depth, which was used to calculate SE_{HB} between
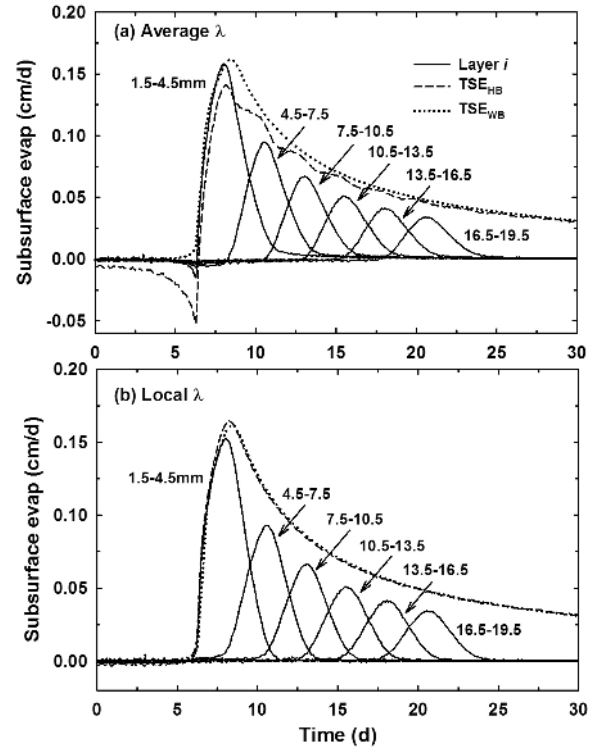
Figure 7. Change of the local subsurface evaporation rates for silt determined by the heat balance method (SE_{HB}, equation (1)) using 3 mm temperature observation grids and (a) average thermal conductivity, and (b) local thermal conductivity. The dark dashed line and dotted line indicate the total subsurface evaporation rate from heat balance (TSE_{HB}) and from water balance (TSE_{WB}, equation (26)) below 1.5 mm depth, respectively.
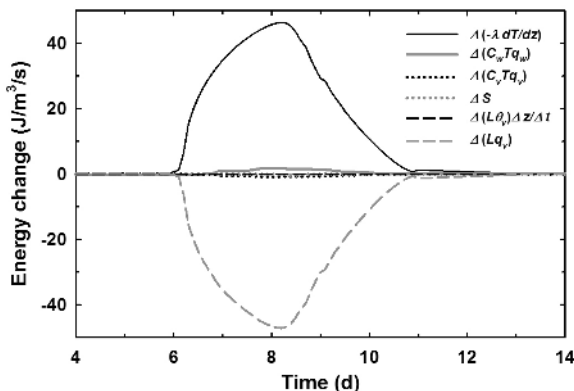
the $1.5-4.5$ mm soil layer, the resulting thermal conductivity was 0.92 W m^{-1} °C^{-1}. However, when computing local values of λ in the $0-3$ mm and $3-6$ mm depths, the results were 0.89 W m^{-1} °C^{-1} and 1.00 W m^{-1} °C^{-1}, respectively. The incoming conduction heat flux into the $1.5-4.5$ mm layer from the lower profile was smaller when using average λ since it was less than λ in the $3-6$ mm layer. The outgoing conduction heat flux from the $1.5-4.5$ mm layer toward the surface was larger when using average λ, since it was greater than λ in the $0-3$ mm layer. Hence, using an averaged λ made the increase of sensible heat in the $1.5-4.5$ layer smaller than when using a local (or depth-specified) λ, resulting in underestimation of subsurface evaporation rate. To correct this error, equation (1) can be modified as follows;

$$LE = \left[\left(-\lambda_{i+1/2} \frac{T_i - T_{i+1}}{z_i - z_{i+1}} \right) - \left(-\lambda_{i-1/2} \frac{T_{i-1} - T_i}{z_{i-1} - z_i} \right) \right] - \Delta S,$$

$$(27)$$

where $\lambda_{i+1/2}$ and $\lambda_{i-1/2}$ are the thermal conductivities between depth z_{i+1} and z_i, and between depth z_{i-1} and z_i in Figure 1, respectively. Figure 7b shows calculated local and total subsurface evaporation rates for silt using equation (27). Calculated TSE_{HB} in equation (27) had no negative values, showing that the maximum value at day 7

increased from 0.15 cm d^{-1} to 0.17 cm d^{-1} and agreed well with the TSE$_{WB}$. This illustrates how using space-averaged λ induces errors in estimation of subsurface evaporation rates and how using locally determined λ can improve estimation of evaporation. Although λ is measured by the heat-pulse probe as an average value of the probe area [*Yang and Jones*, 2009], tri-needle [*Ren et al.*, 2000] or penta-needle probes [*Endo and Hara*, 2007; *Yang and Jones*, 2009] have the potential to estimate depth-specified λ instead of averaging over paired thermistors above and below heater needles as shown in Figure 1. The following discussion is based on the calculations resulting from equation (27).

[33] While the soil heat flux is defined only by the conduction phase in equation (1), a more detailed treatment of soil heat flux may include the summation of: (1) conduction of sensible heat, (2) sensible heat by convection of liquid water and (3) water vapor, and (4) latent heat transfer by vapor flow as described in equation (5) [*de Vries*, 1958]. The differences between incoming and outgoing heat flux in the 1.5−4.5 mm soil increment (for silt soil) were compared to observe the impact when calculating subsurface evaporation rates (Figure 8). Differences in properties at adjacent sensing nodes include, $(C_w T q_w)_{i+1/2} - (C_w T q_w)_{i-1/2}$, $(C_v T q_v)_{i+1/2} - (C_v T q_v)_{i-1/2}$, and $(Lq_v)_{i+1/2} - (Lq_v)_{i-1/2}$ corresponding to $(-\lambda dT/dz)_{i+1/2} - (-\lambda dT/dz)_{i-1/2}$ in Figure 1. When evaporation occurred in this 1.5−4.5 mm soil increment from day 6 to day 11 (Figure 7b), the latent heat by vapor-phase flow (Lq_v) exhibited large negative values indicating energy was exiting by evaporation, and the conduction phase $(-\lambda dT/dz)$ had large positive values indicating the main source supplying energy for water vaporization. The sensible heat by convection of the vapor-phase and sensible and latent heat storage phases were negligibly small. Although the convection of liquid-phase water showed small positive values, it was approximately 3% of the conduction phase because of the small liquid-phase flux at the drying front (i.e., less than 0.1 cm d^{-1}). When calculating the subsurface evaporation rate, heat convection of the

liquid-phase was less sensitive compared to the conduction phase, and ΔS in equation (1) was also negligibly small. In the field measurement shown in *Heitman et al.*, [2008b], the change of ΔS was much smaller than the change of conduction phase, which is consistent with the results shown in our study.

3.1.5. Impact of Temperature Observation Grid Spacing and Soil Texture on the Heat Balance Method

[34] Figure 9 shows various calculated results of total subsurface evaporation rate from the heat balance method (TSE$_{HB}$, equation (27)) comparing results from 1, 3 and 6 mm temperature observation grids. Also included is the total surface/subsurface evaporation obtained from combined liquid- (LPF) and vapor-phase fluxes (VPF) emitted from the soil surface (Figures 4a−4c). Remembering LPF represents water flux evaporating at the soil surface into the atmosphere, VPF therefore represents the total subsurface evaporation rate. During stage 1 evaporation, the TSE$_{HB}$ with observation grids of 1, 3, and 6 mm all agreed with VPF estimates near zero cm d^{-1} for sand and silt, but beginning with stage 2 evaporation, diminished correlations arose for all texture types and grid spacings. The large discrepancies found at the beginning of stage 2 evaporation were evident for each of the three soils with greater differences exhibited for the finer textured soil and larger spacing. By the end of the 30 day simulations, cumulative subsurface evaporation estimate disagreements between total subsurface evaporation rate (VPF) and TSE$_{HB}$ were similar in sand and silt being on the order of 16, 24, and 34% for 1, 3, and 6 mm spaced grids, respectively. In silty clay error estimates were 25, 50, and 69% for the 1, 3, and 6 mm grid calculations, respectively. These discrepancies were largely the cause of the "undetectable zone" within the soil profile extending from the surface down to the first midpoint of the prescribed grid spacing (i.e., sensor spacing). Assuming the top temperature sensor is located at the soil surface ($z_1 = 0$ in Figure 1), equation (1) cannot account for half of the top observation grid. Hence subsurface evaporation between the surface and 0.5, 1.5, and 3 mm depths cannot be detected for 1, 3, and 6 mm grids, respectively (Figure 6). This indicates that by using finer observation grids close to the soil surface makes the undetectable zone smaller and makes the subsurface evaporation estimation possible from earlier time after stage 2 evaporation started.

[35] The discrepancies in accounting for subsurface evaporation were truncated for coarse textured soil and lasted longer for fine textured soil (Figure 9). In the case of the 6 mm grid, the discrepancy occurred from days 5.5 to 9 for sand, from days 6 to 11 for silt, and from days 0 to 20 (not shown in Figure 9c) for silty clay. Differences in the drying front speed of descent for each soil texture determine the temporal extent of this disagreement. Under the same atmospheric conditions, the speed of descent in sand is faster than silty clay and the drying front goes deeper below the undetectable zone (Figure 6). This indicates that the heat balance method for subsurface evaporation estimation is more applicable for coarse textured soils than finer textured soils and furthermore, corrections or additional algorithms that account for evaporation in the undetectable zone are needed to reduce the extent of this discrepancy.
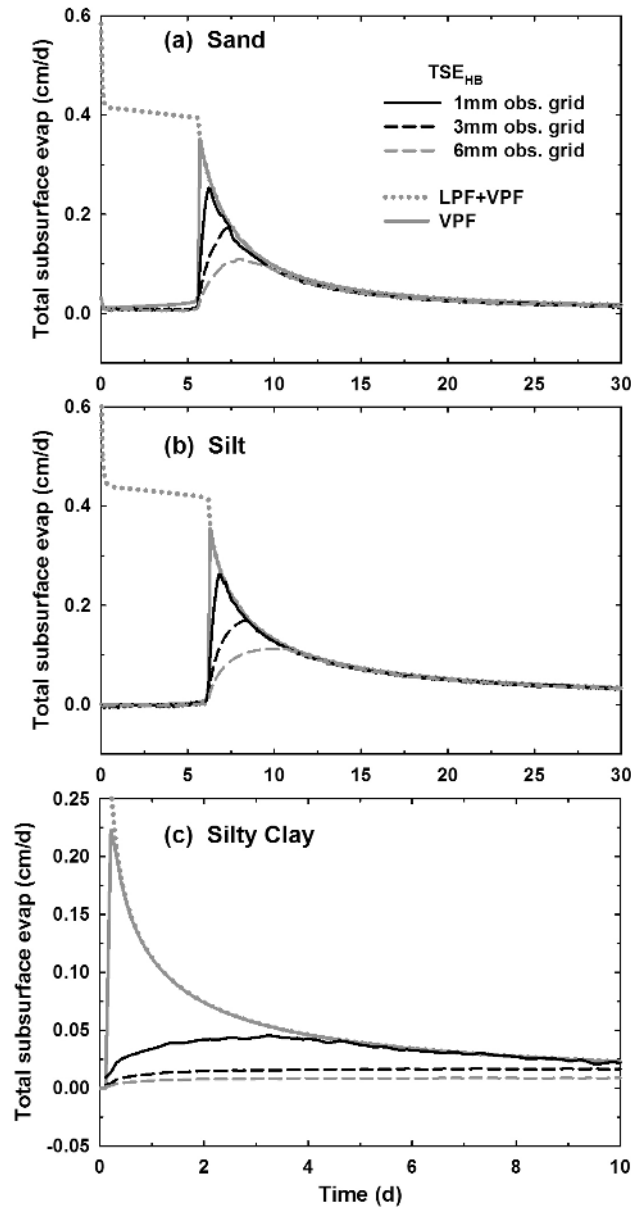

Figure 8. Components of energy change in a soil layer of 1.5−4.5 mm during subsurface evaporation of silt (dark solid line: conduction, light solid line: convection of liquid water, dark dotted line: convection of water vapor, light dotted line: sensible heat storage, dark dashed line: latent heat storage, light dashed line: latent heat flow).

Figure 9. Total subsurface evaporation rates determined by heat balance (TSE$_{HB}$, equation (27)) for each temperature observation grid (1, 3, and 6mm) for (a) sand, (b) silt, and (c) silty clay. Light dotted lines and light solid lines show surface evaporation rate (LPF+VPF) and surface vapor-phase flux (VPF), respectively. Note Figure 9c is plotted at 1/3 the temporal scale for emphasis of the early conditions.

3.2. Evaporation Simulation With Diurnal Boundary Condition

3.2.1. Simulated Soil Surface Flux and Soil Temperatures

[36] Figure 10a shows individual liquid- (LPF, $q_w(0, t)$) and vapor-phase fluxes (VPF, $q_v(0, t)$) exiting the soil surface, simulated in silt soil under diurnal atmospheric boundary conditions. For all simulated days, evaporation rates were maximum at noon corresponding with incoming solar radiation peaks (Figure 2), and minimum was between midnight and early morning. It is evident that solar radiation was the main force of soil water evaporation [*Penman*, 1941; *Fritton et al.*, 1970]. The initial pressure head of the

soil profile simulation was relatively high (-100 cm), resulting in high evaporation rates for the first few days of simulation (1.4 cm d^{-1} at day 0.5) with reduced rates in time (0.1 cm d^{-1} at day 19.5). The LPF was the dominant source of evaporation with water vaporization at the soil surface occurring for 2.5 days before subsurface vaporization began. Between days 2 and 10 LPF is the dominant source early in the day and VPF took over for the rest of the day with some overlap where both LPF and VPF occurred simultaneously. This indicates the soil profile was wet enough to supply water toward the soil surface overnight and into the morning. But the reduction in soil water content by evaporation near the surface meant the drying front
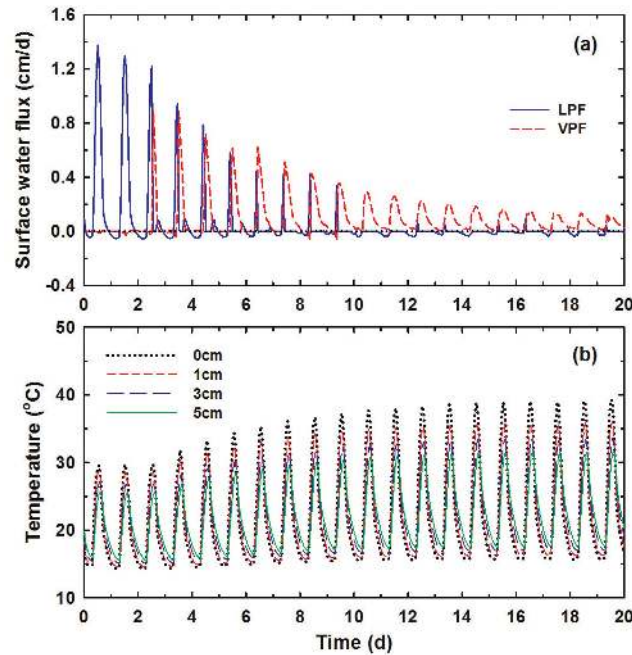
Figure 10. Simulated (a) soil surface water flux with components of liquid- (LPF) and vapor-phase fluxes (VPF), and (b) soil temperature change under diurnal atmospheric cycles.

penetrated deeper with time and vaporization occurred more in the subsurface. Small increases of LPF were found in the late afternoon (e.g., day 2.7), meaning there was some rewetting of the soil surface from below as a result of reduced atmospheric evaporation demand [*Novak.*, 2010]. After 10 days, VPF was the sole evaporation source meaning all of the vaporization occurred within the subsurface. Figure 10a shows negative values of LPF during midnight to morning time suggesting water vapor condensation at the soil surface. Since VPF values were close to zero in the early morning, vapor in the atmosphere condensed mainly on the soil surface.

[37] Simulated soil temperatures are shown in Figure 10b where for all the simulation days, the temperature at the soil surface was maximum around 1 pm based on the maximum solar radiation at noon and the maximum air temperature at 1 pm (Figure 2). The minimum temperatures occurred around 5 am based on the minimum air temperature at 1 am and no solar radiation at night. Temperatures at shallower depths were larger than deeper depths during daytime and smaller in the nighttime. The daily temperature amplitudes were smaller initially, because the heat capacity of soil was higher because of higher water contents and heat depletion by evaporation was larger.

3.2.2. Diurnally Varied Subsurface Evaporation Estimates Using the Heat Balance Method

[38] Using the same procedure as described for constant atmospheric conditions (section 3.1.3), subsurface evaporation rates were calculated using the heat balance method (equation (1) or equation (27)) using calculations of soil temperature and thermal properties (λ and C) from simulated water contents. The 1, 3, and 6 mm temperature observation grid spacings were evaluated and here we begin by showing results from the 3 mm spacing. Figure 11a shows spatial and temporal variation in the calculated local subsur-

face evaporation rates from heat balance (SE_{HB}) for each of three soil depth increments defined by the 3 mm temperature observation grid (i.e., $1.5-4.5$, $4.5-7.5$, and $7.5-10.5$ mm). In this case, local (depth-specified) λ was used for estimating SE_{HB} (equation (27)). During the initial 2.5 days, SE_{HB} was nearly zero since all of the evaporation occurred at the soil surface or above the undetectable 1.5 mm zone. The SE_{HB} resulting from the $1.5-4.5$ mm layer was greater than the deeper layers from day $2.5-13.5$. The SE_{HB} from $4.5-7.5$ mm began to exceed evaporation from $1.5-4.5$ mm after day 13.5. The $7.5-10.5$ mm zone became the dominant layer for evaporation after day 16.5. This shifting pattern is similar to field measurement results shown in *Heitman et al.* [2008b].

[39] The total subsurface evaporation rates from the heat balance method (TSE_{HB}) between 1.5 mm to 100 mm are plotted in Figure 11b as well as the total subsurface evaporation rate from water balance estimates (TSE_{WB}, equation (26)) for all depths down to 100 mm, excluding the soil surface. In Figure 11b, two TSE_{HB} calculated using the average λ and the local λ are shown for comparison. From day 2.5 to 7.5, the TSE_{HB} from with local λ, underestimated TSE_{WB}, indicating that subsurface evaporation was occurring in the undetectable zone from 0 to 1.5 mm depth. After day 7.5, TSE_{HB} agreed well with TSE_{WB}, suggesting that after the drying front progresses below the undetectable zone (i.e., below 1.5 mm depth) the heat balance method provides reasonable estimates of subsurface evaporation rates using local estimates of λ.

[40] Meanwhile, using the heat balance method with averaged λ substantially overestimated the TSE_{HB} compared with daytime estimates of TSE_{WB} and underestimated nighttime predictions compared with TSE_{WB}. These negative evaporation rates, also seen in *Heitman et al.* [2008a, 2008b], indicate condensation occurring within the
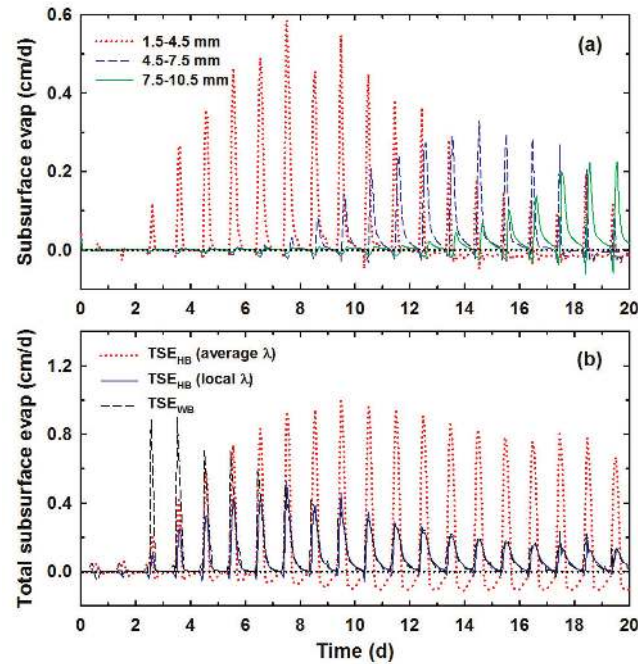
Figure 11. (a) Change in local subsurface evaporation rates under diurnal atmospheric cycles determined by the heat balance method (SE_{HB}, equation (27)) using 3 mm temperature observation grids and local thermal conductivity (λ), and (b) comparison between total subsurface evaporation rate from heat balance (TSE_{HB}) using average λ (dotted line), using local λ (solid line), and from water balance (TSE_{WB}, dashed line).

subsurface. Based on this comparison using numerical simulation, the nighttime condensation arises from averaging of λ and is virtually nonexistent when space-averaged λ is used. To illustrate this important concept in greater detail, we focus in on the 1.5–4.5 mm soil layer between day 8 and 10 in Figure 11a and plot the temporally varying average λ between 0–6 mm along with local λ for 0–3 mm and 3–6 mm in Figure 12a. We also plot temporal variation in the conduction component of energy (first term on the right-hand side of equations (1) or (27)) and in the sensible heat storage component of energy (equation (2)) for the 1.5–4.5 mm soil layer shown in Figure 12b. Since there was no irrigation or rainfall in this simulation, the soil profile was generally drier close to the surface and wetter deeper in the profile. Corresponding to these water content conditions, the locally derived λ between 0 and 3 mm was smaller than the locally determined λ between 3 and 6 mm, where the largest differences occurred in the afternoon. The averaged λ naturally fell between these two local λ values. Daytime soil temperatures were maximum at the surface and cooler in the profile (Figure 10b), generating downward conduction heat flux. This downward conduction heat flux was smaller using the local λ than when average λ was used in calculations because average λ was larger than local λ between the 0–3 mm depth. By contrast, the conduction heat flux going out from the layer was larger in case of local λ than average λ, because local λ for the 3–6 mm layer was larger than average λ. Because of these conduction heat flux differences, the increase in sensible heat within the 1.5–4.5 mm layer (Figure 12b) was much larger for average λ compared with local λ, resulting in overestimation of the subsurface evaporation rate.

[41] Meanwhile during late afternoon and nighttime (i.e., day 8.7–9.3), temperature gradients were reversed and the direction of conduction heat flux was upward to the surface. The incoming heat flux to the layer from the lower profile was larger in the case of local λ than for average λ because local λ was larger in the 3–6 mm layer, and the outgoing heat flux from the layer to the soil surface was smaller in the case of local λ than for the average λ since local λ in the 0–3 mm layer was smaller. This created the smaller (sometimes negative) increase in sensible heat within the layer for the case of average λ and the resulting underestimation of subsurface evaporation rate. The change of sensible heat storage, ΔS, was much smaller than the change by conduction heat flux, which is consistent with the results of our simulation using a constant atmospheric boundary condition (Figure 8) and with field measurements presented in *Heitman et al.* [2008b]. Hence, accurate determination of λ appears to be the most important component in calculations of the heat balance method. As suggested in section 3.1.4, using measurements of local (depth-specified) λ with tri-needle HPP or penta-needle HPP appears to significantly improve estimation of subsurface evaporation rate using the heat balance method.

3.2.3. Comparison of Daily Evaporation

[42] Total subsurface evaporation rate from the heat balance method were calculated for 1, 3, and 6 mm temperature observation grids using local λ. Figure 13 shows the daily total evaporation estimates (daily sum of Figure 11b) using the heat balance method (TSE_{HB}) as well as daily total evaporation based on the water balance (TSE_{WB}) in addition to the total daily evaporation (daily sum of Figure 11a). The total evaporation was 0.32 cm on day 1 and decreased with
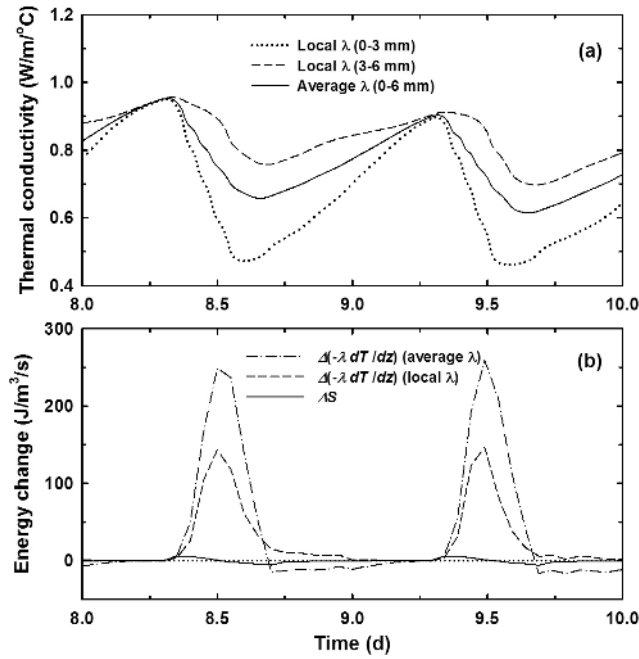
Figure 12. (a) Local and average thermal conductivity in the $0-6$ mm depth and (b) components of sensible energy change in the $1.5-4.5$ mm soil layer under diurnal atmospheric cycling during days $8-10$.

time down to 0.05 cm d^{-1} on day 20. The computed TSE$_{WB}$ was smaller than the total evaporation until the 10th day because water vaporization occurred at the soil surface as well as within the subsurface (surface and transient evaporation stage). Beyond day 10, the TSE$_{WB}$ was consistent with the total evaporation (subsurface evaporation stage). The TSE$_{HB}$ results were underestimated compared with TSE$_{WB}$ initially because of the "undetectable zone". As expected, TSE$_{HB}$ estimates using smaller observation grid spacing approach the TSE$_{WB}$ earlier because of the smaller undetectable zone. Predictions of TSE$_{HB}$ with 1, 3, and 6 mm grid spacing complied with TSE$_{WB}$ after 8, 10, and 12 days, respectively. This result endorses the use of HPP with smaller spacings at least near the soil surface where the undetectable zone can be minimized, leading to more accurate estimates of total subsurface evaporation rate. Although this simulation required 10 days before all of the water va-

porization took place in the subsurface, we note that the speed of the drying front descent will vary with soil texture (i.e., coarse texture is faster as shown in Figure 6) and atmospheric forcing conditions (i.e., higher wind speed, lower humidity, or larger solar radiation increasing evaporation rate). For example, in the field measurements shown in *Heitman et al.* [2008b], subsurface evaporation was detected by the heat balance method only 3 days after irrigation.

[43] Daily TSE$_{HB}$ with a 3 mm observation grid and using the average λ estimate is also plotted in Figure 13. Based on the simulated soil texture, λ, water content and atmospheric boundary conditions in this study, estimates of subsurface evaporation derived using the average λ were almost double the estimate from TSE$_{WB}$ after 10 days (also see Figure 11b). However, in *Heitman et al.* [2008b], good agreement was shown between daily evaporation rate from the heat balance method using a 6 mm observation grid
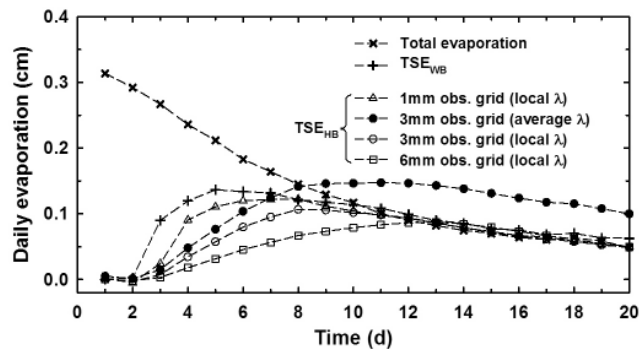
Figure 13. Comparison of daily evaporation obtained by total evaporation (water flux) at the soil surface ($\times$) and total subsurface evaporation based on a water balance ($+$, TSE$_{WB}$). In addition, heat balance (TSE$_{HB}$) based estimates are given for both local and average λ using 3 different grid (sensor) spacings.

with an average λ estimate and the daily evaporation rates independently measured using microlysimeter and Bowen ratio methods. Since our simulation conditions differed from the field conditions of *Heitman et al.* [2008a, 2008b] comparisons described here are limited and readers should be aware that additional factors not considered in simulations may impact daily evaporation rate estimates under field conditions. Therefore, results of these numerical simulations and the suggestion that local λ rather than average λ yield more accurate estimates of subsurface evaporation rate from the heat balance method need to be further studied and verified with additional laboratory and field experiments.

4. Summary

[44] In this study, the applicability and potential limitations of the heat balance method for determining in situ subsurface soil water evaporation rate was evaluated. It was based on measured or estimated soil temperature and thermal properties using a heat-pulse probe (HPP). First, soil temperatures, water contents, and thermal properties generated from soil water evaporation simulations under constant atmospheric boundary condition were used to estimate subsurface evaporation rates using the heat balance method (SE_{HB}). The SE_{HB} values calculated in each soil layer, where segregated by observation node spacing related to what would be the temperature sensor spacing if the method were applied experimentally. Shallower layers exhibited larger SE_{HB} values in the early stages of subsurface evaporation while deeper layer estimates revealed smaller values later on, corresponding to the drying front deepening and evaporation rates decreasing with time. Since SE_{HB} is an indirect estimate, it was evaluated by comparing to directly determined subsurface evaporation rate calculations from a water balance (SE_{WB}). Results of SE_{HB} underestimated those from SE_{WB} when averaged thermal conductivity, λ, was used for heat balance calculations. This is especially true when there is a large λ gradient at the drying front (i.e., smaller λ above and larger λ below), where the average λ causes an underestimation of sensible heat increase by conduction heat flux in the layer. A modification using local (or depth-specified) λ instead of average λ was suggested to improve subsurface evaporation estimation. The impact of soil thermal components on estimation of subsurface evaporation rate was also investigated. The conduction phase was shown to be the main component supplying energy for soil water vaporization, while convection of liquid water flux was only about 3% of the conduction phase because of the small liquid water flux, i.e., less than 0.1 cm d^{-1} at the drying front. Even the change in sensible heat storage component (ΔS in equation (1)) was negligibly small. It is therefore obvious that accurate measurement of thermal conductivity using the HPP is more critical than measurement of heat capacity for accurate estimation of subsurface evaporation using the heat balance method supported through HPP measurements.

[45] The impacts of temperature observation grid (sensor) spacing (1, 3, and 6 mm) and soil texture (sand, silt, and silty clay) on subsurface evaporation estimation were also investigated. The heat balance method includes an "undetectable zone" within the soil profile extending from the soil surface down to the midpoint of the first temperature observation grid point (sensor). A key to estimating total subsurface evaporation more accurately early on after initiation of stage 2 evaporation, was to minimize the depth of the undetectable zone and the time evaporation occurs within it. The speed of drying front decent downward into the soil was faster in sand than in silt and in silty clay using similar surface boundary conditions. Corresponding to these effects, differences between simulated total subsurface evaporation and SE_{HB} were smallest for sand with a 1 mm observation grid and largest for silty clay with a 6 mm grid. These results theoretically demonstrate that finer spacing, (i.e., 1 mm) provides improved accuracy of subsurface evaporation estimation than coarse (i.e., 6 mm), and therefore, developing a HPP with smaller temperature sensor spacing close to the soil surface should improve measurement resolution. Furthermore, the heat balance method yields better results in coarse textured soils (sand or silt in this study) than in finer textured soils in part because there may be sustained evaporation (combined surface and subsurface) within the undetectable zone.

[46] Second, a simulation with diurnal atmospheric cycling was conducted to test the applicability of the heat balance method to more field-like conditions. Calculated SE_{HB} values were at maximum around midday and near zero at night corresponding to daily cycles of air temperature, relative humidity, and solar radiation. As with the constant boundary conditions, the overlapping contributions of each soil layer in which SE_{HB} was computed are seen in time to diminish in magnitude with depth. The comparison of SE_{HB} using average λ with the water balance–based subsurface evaporation rate estimates (SE_{WB}) revealed substantial overestimation during the day and underestimation (sometimes showing negative values) at night. Again, these discrepancies are associated with large λ gradients at the drying front. During daytime when surface temperature was maximum and conduction heat flux direction was downward, the sensible heat increase by conduction heat flux was overestimated, as was soil layer subsurface evaporation rate when using average λ. Minimum surface temperature causing upward conduction heat flux at night was associated with underestimation of sensible heat increase in the soil layer and underestimation of evaporation rate. The use of local λ for SE_{HB} estimates instead of average λ substantially improved the agreement between SE_{HB} and SE_{WB} estimates. On the basis of these simulation results, we suggest two improvements to HPP-based estimates of subsurface evaporation; (1) reduction of the "undetectable zone" using closer temperature sensing spacing near the surface, and (2) use of locally determined λ between each heater needle and temperature sensor needle in place of averaging λ across both sides of a heater needle. These adjustments to the heat balance method for subsurface evaporation should improve the accuracy of laboratory- and field-based estimates.

References

Bristow, K. L. (1998), Measurement of thermal properties and water content of unsaturated sandy soil using dual-probe heat-pulse probes, *Agric. For. Meteorol.*, *89*, 75–84.

Camillo, P. J., and R. J. Gurney (1986), A resistance parameter for bare-soil evaporation models. *Soil Sci.*, *141*, 95–105.

Campbell, G. S. (1985), *Soil Physics with Basic, Transport Model for Soil-Plant Systems*, Elsevier, New York City, N. Y.

Campbell, G. S., C. Calissendorff, and J. H. Williams (1991), Probe for measuring soil specific heat using a heat-pulse method, *Soil Sci. Soc. Am. J.*, *55*, 291–293.

Carsel, R. F., and R. S. Parrish (1988), Developing joint probability distributions of soil water retention characteristics, *Water Resour. Res.*, *24*(5), 755–769.

Chen, P., and D. C. T. Pei (1989), A mathematical model of drying processes, *Int. J. Heat Mass Transfer*, *32*(2), 297–310.

Chung, S.-O., and R. Horton (1987), Soil heat and water flow with a partial surface mulch, *Water Resour. Res.*, *23*(12), 2175–2186.

Coumans, W. J. (2000), Models for drying kinetics based on drying curves of slabs, *Chem. Eng. Proc.*, *39*(1), 53–68.

de Vries, D. A. (1958), Simultaneous transfer of heat and moisture in porous media, *Trans. Am. Geophys. Union*, *39*(5), 909–916.

Endo, A., and M. Hara (2007), Simultaneous measurement of water flux density vectors and thermal properties under drainage conditions in soils, *Paddy Water Environ.*, *5*, 171–180.

Evett, S. R., A. W. Warrick, and A. D. Matthias (1995), Wall material and capping effects on microlysimeter temperatures and evaporation, *Soil Sci. Am. J.*, *59*, 329–336.

Fayer, M. J., and C. S. Simmons (1995), Modified soil water retention functions for all matric suctions, *Water Resour. Res.*, *31*(5), 1233–1238.

Forsythe, W. E. (1964), Smithsonian physical table, Smithsonian Institution Publication 4169, Washington, DC.

Fritton, D. D., D. Kirkham, and R. H. Shaw (1970), Soil water evaporation, isothermal diffusion, and heat and water transfer, *Soil Sci. Soc. Am. J.*, *34*, 183–189.

Heitman, J. L., R. Horton, T. J. Sauer, and T. M. DeSutter (2008a), Sensible heat observations reveal soil-water evaporation dynamics, *J. Hydrometeorol.*, *9*, 165–171, doi:10.1175/2007JHM963.1.

Heitman, J. L., X. Xiao, R. Horton, and T. J. Sauer (2008b), Sensible heat measurements indicating depth and magnitude of subsurface soil water evaporation, *Water Resour. Res.*, *44*, W00D05, doi:10.1029/2008WR006961.

Jensen, M. E., R. D. Burman, and R. G. Allen (1990), Evapotranspiration and irrigation water requirements, *ASCE Manuals Rep. Eng. Pract.*, *70*, Am. Soc. Civ. Eng.SC, New York City, N. Y.

Jury, W., and R. Horton (2004), *Soil Physics.* 6th ed., John Wiley, Hoboken, N. J.

Kaviany, M., and M. Mittal (1987), Funicular state in drying of a porous slab, *Int. J. Heat Mass Transfer*, *30*(7), 1407–1418.

Keey, R. B. (1972), *Drying Principles and Practice*, Pergamon, New York City, N. Y..

Kirkham, D., and W. L. Powers (1972), *Advanced Soil Physics*, Elsevier, New York City, N. Y.

Kluitenberg, G. J., T. E. Ochsner, and R. Horton (2007), Improved analysis of heat pulse signals for soil water flux determination, *Soil Sci. Soc. Am. J.*, *71*, 53–55.

Lehmann, P., S. Assouline, and D. Or (2008), Characteristic lengths affecting evaporative drying of porous media, *Phys. Rev. E*, *77*(5), 56309.

Mayocchi, C. L., and K. L. Bristow (1995), Soil surface heat flux: some general questions and comments on measurements, *Agric. For. Meteorol.*, *75*, 43–50.

Mualem, Y. (1976), A new model for predicting the hydraulic conductivity of unsaturated porous media, *Water Resour. Res.*, *12*(3), 513–522.

Nassar, I. N., A. M. Globus, and R. Horton (1992), Simultaneous soil heat and water transfer, *Soil Sci.*, *154*, 465–472.

Novak, M. D. (2010), Dynamics of the near-surface evaporation zone and corresponding effects on the surface energy balance of a drying bare soil, *Agric. For. Meteorol.*, *150*(10), 1358–1365.

Penman, H. L. (1941), Laboratory experiments on evaporation from fallow soil, *J. Agric. Sci.*, *31*, 454–465.

Philip, J. R., and D. A. de Vries, (1957), Moisture movement in porous materials under temperature gradients, *Trans. Am. Geophys. Union*, *38*(2), 222–232.

Prat, M. (2002), Recent advances in pore-scale models for drying of porous media, *Chem. Eng. J.*, *86*, 153–164.

Qiu, G. Y., and J. Ben-Asher (2010), Experimental determination of soil evaporation stages with soil surface temperature, *Soil Sci. Soc. Am. J.*, *74*, 13–22.

Ren, T., G. J. Kluitenberg, and R. Horton (2000), Determining soil water flux and pore water velocity by a heat pulse technique, *Soil Sci. Soc. Am. J.*, *64*, 552–560.

Sakai, M., T. Toride, and J. Šimůnek (2009), Water and vapor movement with condensation and evaporation in a sandy column, *Soil Sci. Soc. Am. J.*, *73*, 707–717.

Saito, H., J. Šimůnek, J. W. Hopmans, and A. Tuli (2007), Numerical evaluation of alternative heat pulse probe designs and analysis, *Water Resour. Res.*, *43*, W07408, doi:10.1029/2006WR005320.

Saito, H., J. Šimůnek, and B. P. Mohanty (2006), Numerical analysis of coupled water, vapor, and heat transport in the vadose zone, *Vadose Zone J.*, *5*, 784–800.

Salvucci, G. D. (1997), Soil and moisture independent estimation of stage-two evaporation from potential evaporation and albedo or surface temperature, *Water Resour. Res.*, *33*(1), 111–122.

Scherer, G. W. (1990), Theory of drying, *J. Am. Ceram. Soc.*, *73*(1), 3–14.

Schlünder, E. U. (1988), On the mechanism of the constant drying rate period and its relevance to diffusion controlled catalytic gas phase reactions, *Chem. Eng. Sci.*, *43*(10), 2685–2688.

Schultz, P. (1991), On the falling-rate period, *Chem. Eng. Technol.*, *14*(4), 234–239.

Shokri, N., P. Lehmann, and D. Or (2009a), Characteristics of evaporation from partially wettable porous media, *Water Resour. Res.*, *45*, W02415, doi:10.1029/2008WR007185.

Shokri, N., P. Lehmann, and D. Or (2009b), Critical evaluation of enhancement factors for vapor transport through unsaturated porous media, *Water Resour. Res.*, *38*, W10433, doi:10.1029/2009WR007769.

Šimůnek, J., M. Šejna, H. Saito, M. Sakai, and M. T. van Genuchten (2008), *The HYDRUS-1D software package for simulating the movement of water, heat, and multiple solutes in variably saturated media, Version 4.0, HYDRUS Software Ser. 3*, Dep. of Environmental Sciences, Univ. of California Riverside, Riverside, Calif., USA.

van Bavel, C. H. M., and D. I. Hillel (1976), Calculating potential and actual evaporation from a bare soil surface by simulation of concurrent flow of water and heat, *Agric For. Meteorol.*, *17*, 453–476.

van Brakel, J. (1980) Mass transfer in convective drying, in *Advances in Drying*, edited by A. S. Mujumdar, pp. 217267–, Hemisphere, New York City, N. Y.

van Genuchten, M. T. (1980), A closed-form equation for predicting hydraulic conductivity of unsaturated soils, *Soil Sci. Soc. Am. J.*, *44*, 892–898.

Warrick, A. W. (2002), *Soil physics companion*, CRC Press, New York City, N. Y.

Yamanaka, T., and T. Yonetani (1999), Dynamics of the evaporation zone in dry sandy soils, *J. Hydrol.*, *217*, 135–148.

Yang, C., and S. B. Jones (2009), INV-WATFLX, a code for simultaneous estimation of soil properties and planar vector flux from fully or partly functioning needles of a penta-needle heat-pulse probe, *Comput. Geosci.*, *35*, 2250–2258.

M. Sakai, S. B. Jones, Department of Plants, Soils and Climate, Utah State University, Agricultural Sciences Building, Rm. 158, UMC 4820, Logan, UT 84322, USA. (scott.jones@usu.edu)

M. Tuller, Department of Soil, Water and Environmental Science, University of Arizona, Tucson, AZ 85721, USA.